ACS APPLIED MATERIALS & INTERFACES

www.acsami.org

Research Article

Design of 3D Printed Programmable Horseshoe Lattice Structures Based on a Phase-Evolution Model

Dong Wang, Haipeng Xu, Jinqiang Wang, Chengru Jiang, Xiangyang Zhu, Qi Ge, and Guoying Gu*

Cite This: *ACS Appl. Mater. Interfaces* 2020, 12, 22146–22156

Read Online

ACCESS | Metrics & More | Article Recommendations | Supporting Information

ABSTRACT: By 3D printing lattice structure with active materials, the structures can exhibit shape and functional changes under external stimulus. However, the programmable shape changes of the 3D printed lattice structures are limited due to the complex geometries, nonlinear behaviors of the active materials, and the diverse external stimuli. In this work, we propose a design framework combining experiments, theoretical modeling, and finite element simulations for the controllable shape changes of the 3D printed horseshoe under thermal stimulus. The theoretical model is based on a phase evolution model that combines the geometrical nonlinearity and the material nonlinearity. Results show that the shapes with positive or negative Poisson's ratio and bending intermediate shapes can be programmed by tuning the geometrical parameters and the temperature distribution. This work provides a method to aid the design of 3D printed functional lattice structures and have potential applications in soft robotics, biomedicine, and energy absorbing fields.

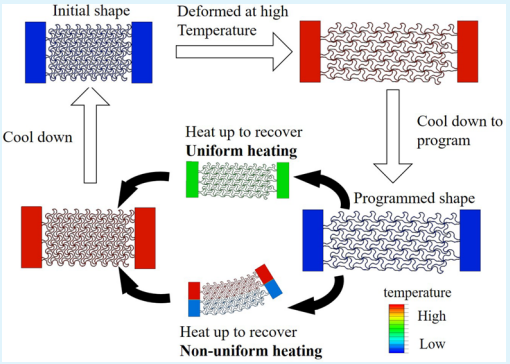

KEYWORDS: *programmable lattice structure, 3D printed shape changing, phase evolution model, negative Poisson's ratio*

INTRODUCTION

Mechanical lattice structures are able to exhibit novel functionalities[1−4] due to their unusual mechanical properties,[5−8] which can be programmed by appropriate design and arrangement of their microstructures. The rapid development of 3D printing technology has enabled the fabrication of complex lattice structures,[7,9,10] which facilitates the physical production of otherwise unrealizable designs with highly ordered 3D structures. However, once manufactured, the arrangement of the unit structures is generally fixed. Thus, the mechanical properties that emerge from the 3D arrangement are not able to be tuned, which significantly limits the application of the lattice structures. In order to overcome this drawback, various approaches of reversible and stiffness tunable structures have been proposed recently.[11−18] Most of them are formed by combining active materials with the 3D printed lattice structures.[19−24] When printing the 3D structures with active materials, the structures have the capabilities of changing their configurations subjected to an external stimulus. 3D printed shape changing lattice structures, with a combination of large recoverable deformations, nonlinearity, and instability, provide promising properties and functionalities and have potential applications, such as in soft robotics,[25−28] aerospace,[29,30] and medical fields.[31]

Despite the diverse achievements, the development of the 3D printed shape changing lattice structures are hindered because of the complex geometries, the large deformation, and the nonlinear material behaviors of the active materials. Thus, the designs of the 3D printed shape changing lattice structures usually rely on empirical methods and lack the guide of theoretical models. To control the shape changing behaviors of the 3D printed lattice structures, several models have been developed. For example, 3D printed auxetic (negative Poisson's ratio) lattice structures that are capable of achieving area changes up to 200% are designed and their shape memory effects are simulated using finite element (FE) simulations.[14] The shape memory effects of 3D printed auxetic lattice structures are studied using finite element simulations, and results show that the moduli and Poisson's ratios could be continuously tailored by tuning the geometrical parameters.[21] However, these models are based on finite element simulations, which are time-consuming, and the fundamental mechanism is difficult to find.[32−35] Recently, analytical models have also been proposed by direct 4D printing via active composite materials driven by the embedded residue stresses.[13,15] But residue stresses are relatively small and large deformation is hard to achieve. Therefore, in order to fully exploit the shape and functional transitions of the 3D printed lattice structures, lattices that could exhibit large and reversible

Received: March 3, 2020
Accepted: April 22, 2020
Published: April 22, 2020

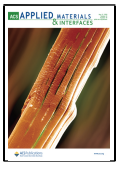

https://dx.doi.org/10.1021/acsami.0c04097
ACS Appl. Mater. Interfaces 2020, 12, 22146−22156

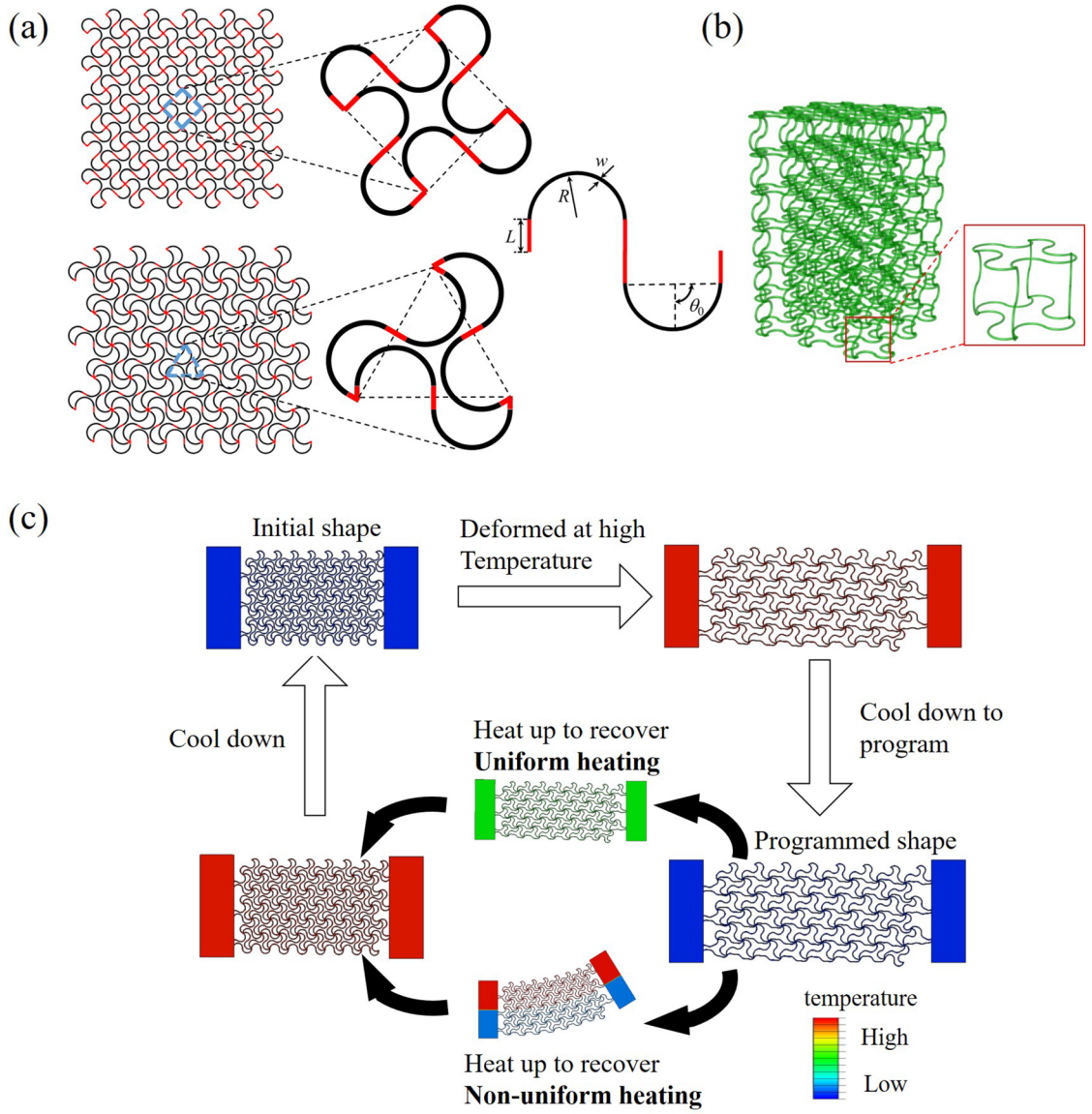

Figure 1. 3D printing of the shape changing lattice structures. (a) Design of the horseshoe lattice. Schematics of a rectangular (upper) and triangular (bottom) horseshoe lattice structures, their representative periodical units, and the single horseshoe microstructure. (b) Structures of a 3 × 3 × 6 3D horseshoe lattice and its periodical unit. (c) Shape memory cycle of the lattice structures. By applying uniform or non-uniform heating in the recovery step, a stretching or bending intermediate shape can be formed.

deformation and analytical models that could predict their behaviors are needed.

In this work, we design 3D printed shape changing rectangular/triangular modified horseshoe lattice structures that can exhibit large controllable deformations subjected to a thermal stimulus. To program their shape changing behaviors, an analytical phase evolution model is developed that takes into account both the geometrical nonlinearity resulting from the large deformation and the material nonlinearity of the thermomechanical material. We also conduct finite element simulations to verify the development. All of the theoretical predicted, FE simulated, and experimental results agree well. By using the theoretical framework, both 3D printed shape changing structures with positive and negative Poisson's ratios are designed. The shape changing behavior of a 3D lattice programmed by axial, bending, or twisting loadings are investigated. Results also show that various intermediate states can be designed by rationally choosing the geometrical design and external stimulus distribution.

DESIGN, EXPERIMENTS, AND MODEL

Geometry of Horseshoe Lattice Structures. Rectangular and triangular modified horseshoe lattice structures are designed as shown in Figure 1a to generate large deformations using material with relatively small failure strain. The structures are constructed by replacing the straight connecting beams in rectangular/triangular lattices with modified horseshoe microstructures. The modified horseshoe microstructure consists of two identical circular arcs arranged antisymmetrically that connected with straight beams. Each circular arc has radius R, arc angle $2\theta_0$, and width w, and the length of each straight beam is L. The thickness of the lattice structure is d. Each modified horseshoe microstructure is constructed on the basis of the horseshoe structure[36] by adding two straight beams to connect the arcs. This modification can significantly improve

https://dx.doi.org/10.1021/acsami.0c04097
ACS Appl. Mater. Interfaces 2020, 12, 22146−22156

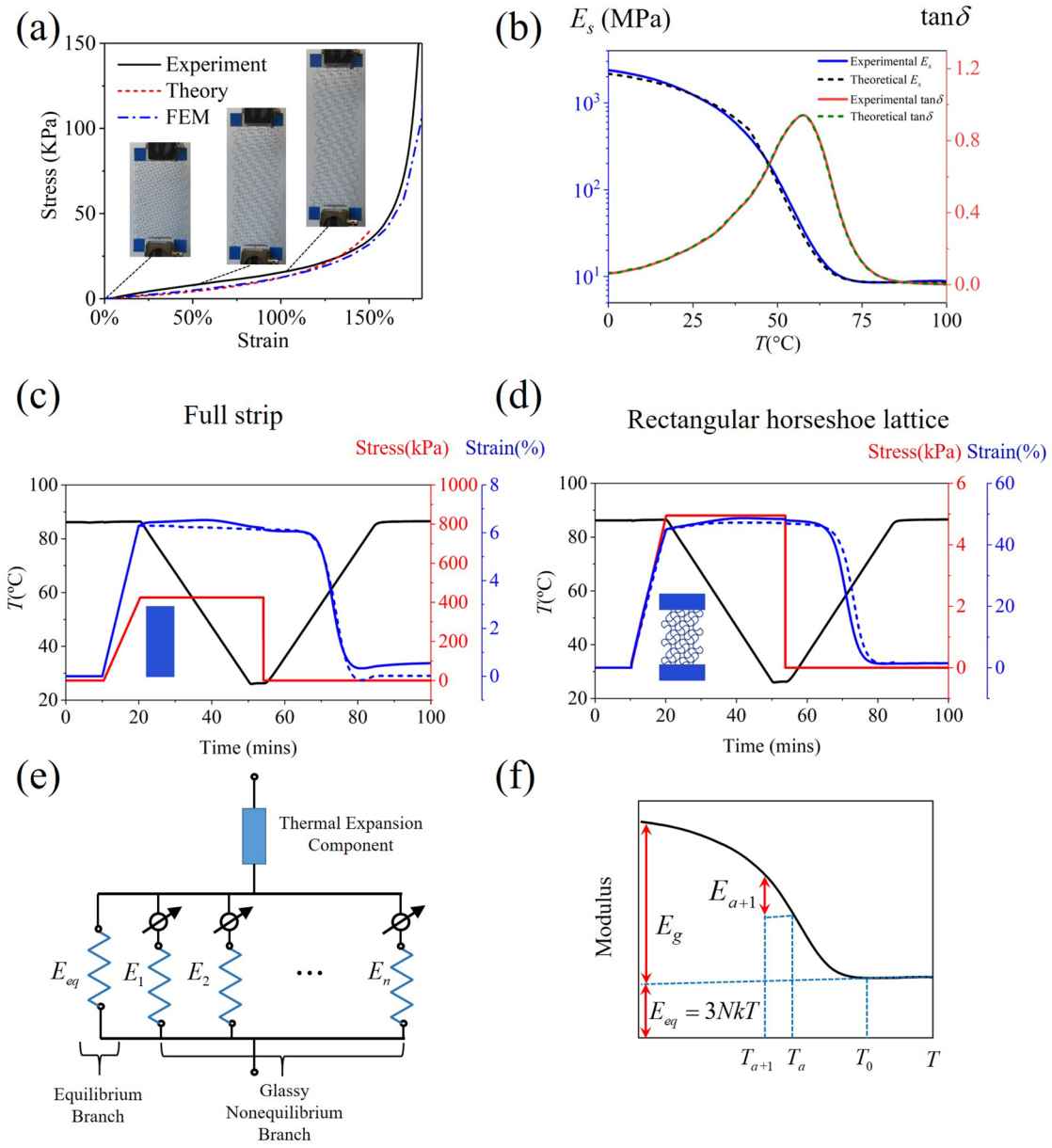

Figure 2. Mechanical properties of the lattice structure. (a) Experimental, theoretical, and FE simulated stress−strain curve of the rectangular lattice under uniaxial tensile test at room temperature (25 °C). (b) Theoretical (dashed) and experimental (solid) storage modulus and tan δ of the shape memory polymer Vero material. (c) A shape memory cycle of a full strip under stress control mode. Inset shows the geometry of the strip. [Experiments, solid curves; model, dashed curves.] (d) Shape memory cycle of a rectangular lattice under stress control mode. Inset shows the geometry of the lattice. (e) Schematic illustration of the phase evolution model for lattice structures. The strain of the lattice structures consists of a thermal expansion component and a mechanical component. The mechanical component consists of an equilibrium branch and n glassy non-equilibrium branches. (f) Schematics of the modulus as a function of temperature. The modulus consists of the equilibrium modulus E_{eq} and the glassy modulus. As the temperature decrease from T_a to T_{a+1}, the increase of glassy modulus is represented by E_{a+1}.

the stretchability of both the single horseshoe microstructure and lattice structures.[37] To avoid cumbersome terminology, the rectangular/triangular modified horseshoe lattice structures are simplified as rectangular/triangular lattices. The structures of a 3 × 3 × 6 3D horseshoe lattice (3 units in x direction, 3 units in y direction, and 6 units in z direction) and its periodical unit are shown in Figure 1b.

By using the shape memory behavior of the lattice materials, the lattice structure can be programmed into different shapes. The shape programming and recovery of the lattice structure are shown in Figure 1c. A triangular horseshoe lattice is taken as an example. The triangular lattice structure is first stretched at a high temperature (80 °C). The deformation is maintained while the temperature is decreased to a low temperature (25 °C). The loading is removed at low temperature, and the lattice is programmed. In the recovery step, the lattice is heated back to high temperature and the original shape of the lattice structure is recovered. By applying uniform or non-uniform heating, different intermediate shapes can be formed. For example, a bending shape can be formed by applying non-uniform heating where the temperature at the top half of the triangular lattice increases faster.

Experiments. The lattice structures are fabricated using a commercial 3D printer (Object J750, Stratasys) with the shape

https://dx.doi.org/10.1021/acsami.0c04097
ACS Appl. Mater. Interfaces 2020, 12, 22146−22156

memory polymer (SMP) Vero (Stratasys Inc., Edina, MN, USA). Vero is photopolymerized with an ink containing isobornyl acrylate, acrylic monomer, urethane acrylate, epoxy acrylate, acrylic monomer, acrylic oligomer, and photoinitiator.[19] It is a rigid plastic at room temperature. This material has been widely used to achieve thermally induced shape changes of 3D printed structures. To characterize the material properties of the SMP material and lattices, several experiments are conducted including the following: (1) uniaxial tensile tests for rectangular and triangular lattice structures; (2) DMA tests for the shape memory polymer Vero; (3) shape memory tests for the a full strip made from Vero and rectangular lattice structures composed of 2 (longitudinal) × 2 (transverse) periodical units. Detailed experimental procedures are shown in the Supporting Information.

The experimental stress−strain curve of the rectangular lattice structure under uniaxial tensile test is shown in Figure 2a. The lattice shows a nonlinear stress−strain behavior. Because the strain is relatively small (<∼50%), the effective modulus is low, resulting from the bending of the arc part. As the strain increases, the modulus increases as the microstructure rotates to align to the vertical direction on which the stress is applied. As the lattice is further stretched (strain > ∼150%), the modulus is large because the microstructure mainly undergoes uniaxial stretch. The inset in Figure 2a shows the experimental shapes with strain at around 0, 50%, and 100%, respectively.

The dependences of the storage modulus and tan δ on temperature are presented in Figure 2b. It can be seen that the storage modulus of the Vero material increases more than two orders from ∼10 MPa at T = 80 °C to above 1 GPa at room temperature. The glassy transition temperature T_g of the Vero material is around 58 °C. Theoretical results based on the multibranch thermomechanical model are compared with the experimental DMA results as shown by the dashed curves in Figure 2b (see the Supporting Information for details). It can be seen that the theoretical estimations can capture the experimental storage modulus and tan δ curves within the entire testing temperature range.

Panels c and d of Figure 2 show experimental results (solid curves) of the stress, strain, and temperature with time in a full shape memory cycle for a full solid strip and a rectangular lattice structure under stress control mode. The insets show the corresponding shape used in the experiments. The use of lattice structure can effciently facilitate the shape programming. Under a programming stress of 400 kPa, the full strip can only be stretched to around 6%, while the strain of the programmed lattice is around 50% with a programming stress of 5 kPa.

Theoretical Model. In order to program the shape changing behaviors of the lattice structures, a theoretical model based on phase evolution is developed. The geometrical nonlinearity resulting from large deformation and the dependence of the SMP's stiffness on temperature are taken into account.

Figure 2e shows a rheological representation of the thermomechanical multibranch model that decomposes the total strain into a mechanical part and a thermal part. For the mechanical part in the model, an elastic phase and several glassy phases are arranged in parallel. As the temperature decreases, the glassy phases gradually form. Once a small piece of glassy phase forms, the corresponding switch in Figure 2e turns on. Depending on the thermomechanical conditions, the glassy phases forming at different times may have different deformation histories. As temperature increases, the glassy phases vanish gradually. According to the kinetic description of the heating process, the piece of glassy phase that grows at a later time vanishes first. Once a small piece of glassy phase vanishes, the corresponding switch in Figure 2e turns off and it does not carry load any more.

Starting from the simple Hooke's law that relates the stress σ and strain ϵ of the linear elastic material by its modulus E as $\sigma = E\epsilon$, we assume the relation between the stress $\sigma(T,\epsilon)$ and the strain ϵ of a lattice structure as

$$\sigma(T, \epsilon) = E(T) f(\epsilon) \tag{1}$$

where $E(T)$ represents the dependence of the SMP material's stiffness on temperature, as shown in Figure 2b. $f(\epsilon)$ characterizes the stress−strain relations of the lattice structure. We may mention that $f(\epsilon)$ can characterize the stress−strain relations due to the geometrical nonlinearity under large deformation. The developed model can also be applied for large deformation. The above assumption separates the effects of temperature and large deformation as the temperature determines the material nonlinearity, while large deformation leads to the geometrical nonlinearity. In eq 1, we neglected the higher order terms of $E(T)$, which characterizes the material nonlinearity due to large deformation. This is because the large deformations of a wide range of lattice structures are mainly due to the geometrical design[5,21,36] but not the material nonlinearity. For example, the elongation of horseshoe structures is due to the rotation of the joints[36,37] and the local maximum strain is around ∼3.5% even when the total strain achieves 100% (Figure S8 in the Supporting Information). In origami-based metamaterials, the large stretchability results from the folding and unfolding motions.[38,39] In these examples, even though the overall strain of these structures is large, the local strain is small, and thus material nonlinearity's effect can be ignored. At the special case, $f(\epsilon) = \epsilon$ for a full strip. For the horseshoe lattice, $f(\epsilon) = f(L,R,w,\theta_0,\epsilon)$ is a complex function that takes into account the effect of geometrical parameters, as derived in the Supporting Information.

The strain $\epsilon(T)$ of the lattice structure consists of the mechanical part $\epsilon^M(T)$ and thermal part $\epsilon^T(T)$ as

$$\epsilon(T) = \epsilon^M(T) + \epsilon^T(T) \tag{2}$$

The thermal strain $\epsilon^T(T)$ at $T = T_H$ is set as the reference state; i.e., $\epsilon^T(T_H) = 0$. At an arbitrary temperature T_r, the thermal strain can then be written as

$$\epsilon^T(T_r) = \alpha_r(T_r - T_H) \tag{3}$$

where $\alpha_r = 1.84 \times 10^{-4}/°C$ is the thermal expansion coefficient (CTE) of Vero (Figure S6). The mechanical strain $\epsilon^M(T)$ in each step in a shape memory cycle is shown as follows (detailed derivations under both strain and stress control modes are shown in the Supporting Information).

(a) In step 1, the lattice structure deformed at a high temperature $T = T_H$ with an applied stress σ_0. At $T = T_H$, all of the glassy phases are turned off. Thus, only the equilibrium phase is working: $E(T = T_H) = 3NkT_H$, where N is the cross-link density of the shape memory polymer and k is Boltzmann's constant.[40] From eq 1, the mechanical strain can be solved as

https://dx.doi.org/10.1021/acsami.0c04097
ACS Appl. Mater. Interfaces 2020, 12, 22146−22156

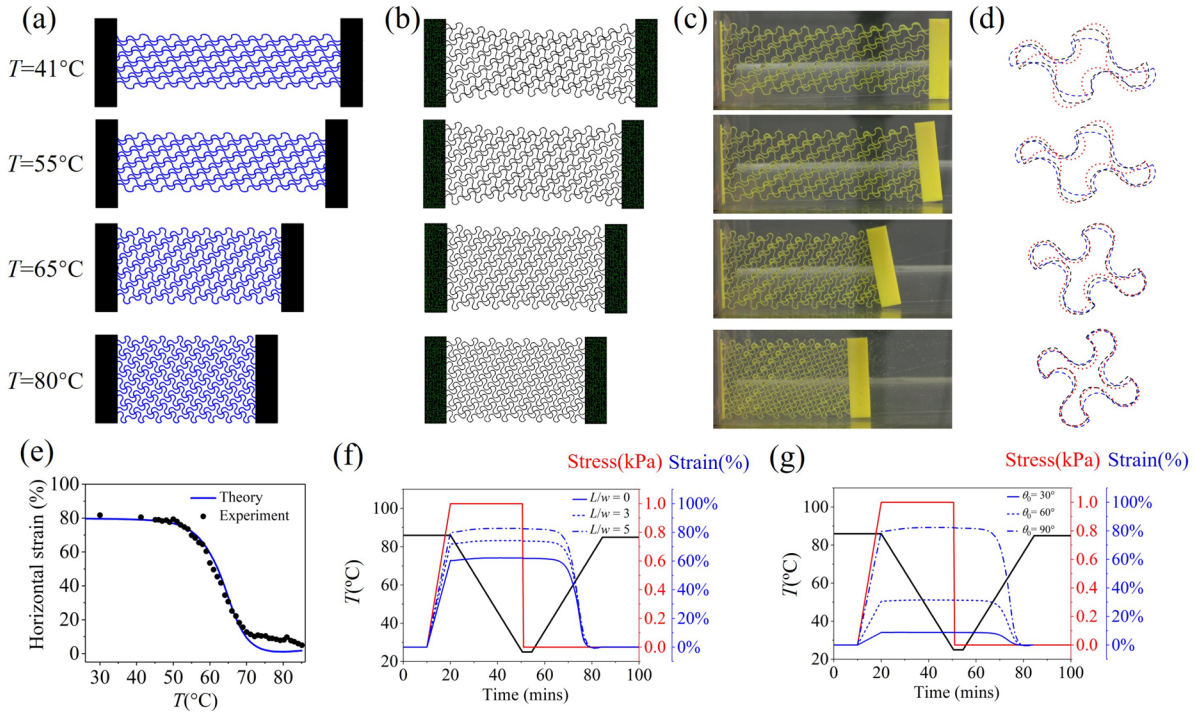

Figure 3. Shape memory behaviors of the rectangular lattice. Comparison of the (a) theoretical predicted, (b) FEM simulated, and (c) experimental shapes of a rectangular lattice at various temperatures in the recovery step. (d) Corresponding theoretical predicted (blue), FEM (red), and experimental (black) shapes of a periodical unit. (e) Experimental and theoretical horizontal strain of the preprogrammed rectangular lattice structure as a function of the temperature in the recovery step. (f, g) theoretical predicted shape memory behaviors of the rectangular lattice with the change of L and θ_0, respectively.

$$\epsilon^{M}(T_H) = f^{-1}\left(\frac{\sigma_0}{3NkT_H}\right) \tag{4}$$

(b) In step 2, temperature decreases from T_H to T_L while holding the applied stress σ_0. As T approaches T_g, new phases are generated one by one. Assuming that as T decreases from T_0 to $T_1 = T_0 - \Delta T_1$, the first glassy phase forms and starts to carry load with the equilibrium branch. $\epsilon^{M}(T_1)$ can be solved as

$$\epsilon^{M}(T_1) = f^{-1}\left(\frac{\sigma_0 + E_1\sigma_0/3NkT_0}{3NkT_1 + E_1}\right) \tag{5}$$

where E_1 is the stiffness of the first glassy branch as shown in Figure 2a.

As T decreases from T_a to $T_{a+1} = T_a - \Delta T_{a+1}$, a new glassy phase ΔE_{a+1} is formed with strain $\Delta\epsilon_{a+1}$. The strains in all working branches, including both elastic and working glassy branch, will change by an amount of $\Delta\epsilon_{a+1}$. The mechanical strain can be calculated as

$$\epsilon^{M}(T_{a+1}) = f^{-1}\left(\frac{\sigma_0 + \sum_{i=1}^{a+1} E_i f(\epsilon_i^0)}{3NkT_{a+1} + \sum_{i=1}^{a+1} E_i}\right) \tag{6}$$

where ϵ_i^0 represents the mechanical strain of the lattice structure when the ith glassy branch starts to work.

(c) In step 3, the holding stress is released at low temperature $T = T_L$. All of the n glassy branches are switched on. After the stress is released, the strain change in each phase $\Delta\epsilon$ can be calculated as

$$\Delta\epsilon = f^{-1}\left(f(\epsilon^{M}(T_L)) - \frac{\sigma_0}{3NkT_L + E_g}\right) - \epsilon^{M}(T_L) \tag{7}$$

where $E_g = \sum_{i=1}^{n} E_i$. The mechanical strain after unloading $\epsilon_u^{M}(T_L)$ is given as

$$\epsilon_u^{M}(T_L) = \epsilon^{M}(T_L) - \Delta\epsilon \tag{8}$$

where $\epsilon^{M}(T_L)$ is obtained by setting $T_{a+1} = T_L$ in eq 6. The shape fixity ratio R_f of the lattice structure, which quantifies the ability of the SMP to fix the programmed geometry after unloading is then calculated as

$$R_f = \frac{\epsilon_u^{M}(T_L)}{\epsilon^{M}(T_L)} \tag{9}$$

(d) In step 4, the temperature increases from T_L to T_H. As the temperature increases, the glassy phases turn off one by one and corresponding strain stored in each glassy phase is released. This process is similar to step 2 except the glassy phases are disconnected one by one.

Finite Element Simulations. To analyze the shape memory effects of the designed lattice structures, finite element (FE) simulations are conducted using the commercial software ABAQUS (3DS Dassault Systemes, France). The thermomechanical behaviors of the SMP as shown in Figure 2b are modeled by the multibranch model. The model parameters obtained in Table S1 are used in FE simulations. The applied boundary conditions are identical to the experiments. The thermally coupled element is used to perform the calculation. The finite element simulation details are shown in the Supporting Information.

https://dx.doi.org/10.1021/acsami.0c04097
ACS Appl. Mater. Interfaces 2020, 12, 22146−22156

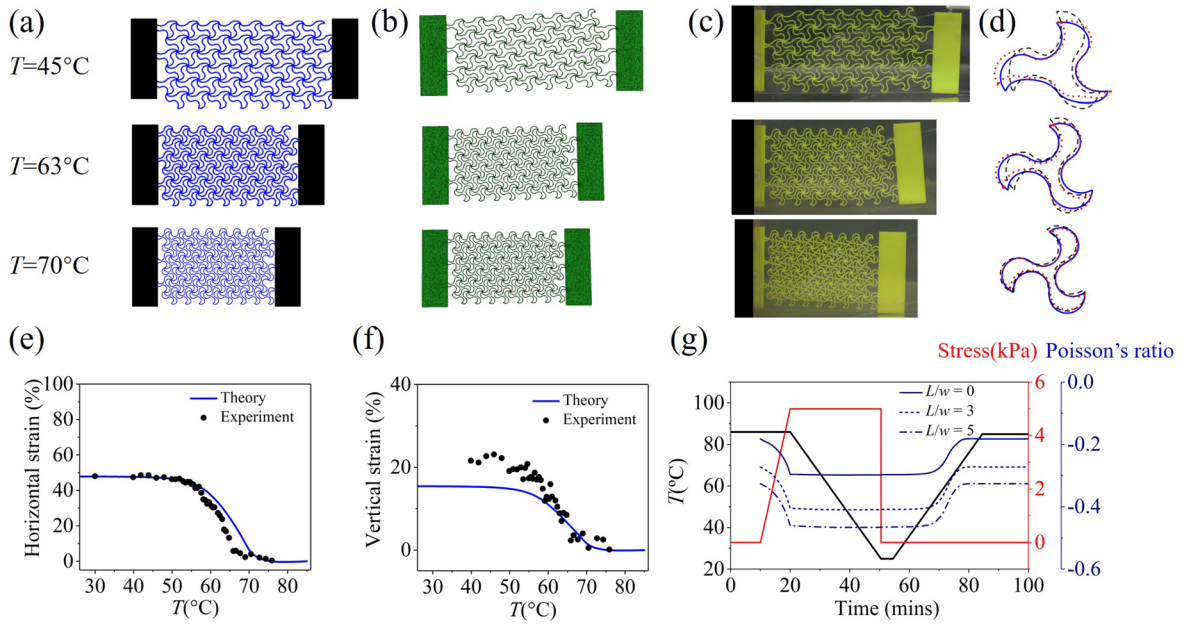

Figure 4. Shape memory behaviors of auxetic triangular lattice. Comparisons of the (a) theoretical predicted, (b) FEM simulated, and (c) experimental deformed shapes of a triangular horseshoe lattice at various temperatures. (d) The corresponding theoretical predicted (blue), FEM (red), and experimental (black) shapes of a periodical unit. Experiments and theoretical predictions of the (e) horizontal and (f) vertical strains of the triangular lattice structures as a function of the temperature at the recovery step. (g) Theoretical predicted Poisson's ratio in a shape memory cycle of the triangular lattice with different L.

RESULTS AND DISCUSSION

Validation of the Theoretical Model. Figure 2a compares the theoretically predicted and FE simulated stress−strain curves of a rectangular lattice under uniaxial tensile stress with the experiments, and they compare well. It indicates that the theoretically derived $f(L,R,w,\theta_0,\epsilon)$ can be used to characterize the geometrical nonlinearity of the rectangular lattice. The theoretical predicted (dashed curves) shape memory behaviors of the rectangular lattice are then compared with the experimental results (solid curves) as shown in Figure 2d. The theoretical predicted shape memory behaviors of a full strip where $f(\epsilon) = \epsilon$ is also shown in Figure 2c. Stress control mode is used. It can be seen that the theoretical results show good agreements with the experiments. However, there is some discrepancy. It may result from the boundary effect of the lattice structure and the hysteresis effect of the SMP material. Interestingly, the theoretical predicted and experimental measured shape recoveries of the rectangular lattices agree better than those of the full solid strip. This is due to the difference of the local strains of both structures in the programming step. Even though the programmed strain for the lattice structure is ∼50%, the local strain of the material is generally smaller than 3% (Figure S8). In contrast, the local strain of the full solid strip equals the programmed strain, which is more than 5% everywhere. Larger local strain in the full solid strip may lead to irreversible plastic deformation and thus lower the shape recovery ratio.

Design of the Rectangular Horseshoe Lattice Structures. The validated model could capture the shape of the lattice structure at various temperatures during a full shape memory cycle and is then used to design the horseshoe lattice structures by tuning the geometrical parameters. Figure 3 presents the theoretical predictions, FE simulations, and the experiments of the recovering shapes of a preprogrammed rectangular lattice structure at various temperatures in the recovery step (Supporting information Videos 1 and 2). The geometrical parameters used are $w = 0.133$ mm, $R/w = 10$, $d/w = 7.5$, $L/w = 5$, and $\theta_0 = \pi/2$. The lattice structure is programmed with an axial strain of 80%. The theoretical predictions of a single periodical unit and the lattice structure by repeating the units along longitudinal and transverse directions are displayed. It should be noted that the theoretical prediction neglects the boundary effect, while the FE simulations take into account the boundary effect as can be seen from Figure 3a,b. Figure 3d compares the deformed shapes of the theoretical, FE simulated, and expeirmental periodical units. The deformed shapes in all of the experiments, theoretical prediction, and FE simulation agree well.

The corresponding quantitatively comparisons of the axial strain between the experimental and theoretical rectangular horseshoe units are shown in Figure 3e. The axial strain in the experiments is chosen as the average axial strain of the two central units. Their coordinates are obtained by ImageJ and then processed by a Matlab code. It can be observed that the theory predicts well the longitudinal strains of the lattice structure at various temperatures. The shapes recover significantly between $T = 50$ and 60 °C in both the experiments and theoretical predictions, which is around the T_g of the Vero material.

Two geometrical parameters L and θ_0 are used to program the shape recovery behavior of the lattice structures in Figure 3f,g, respectively. Other geometrical parameters are fixed. The applied stress is set as 1 kPa. It can be seen that the strain of the lattice structures increases as the length L increases, because the longitudinal strain is mainly due to the rotation of the beams and therefore it is larger for a longer beam. On the other hand, the longitudinal strain decreases as θ_0 decreases from 90° to 30°, as shown in Figure 3g, as the rectangular lattice structure with smaller θ_0 is more difficult to deform.

https://dx.doi.org/10.1021/acsami.0c04097
ACS Appl. Mater. Interfaces 2020, 12, 22146−22156

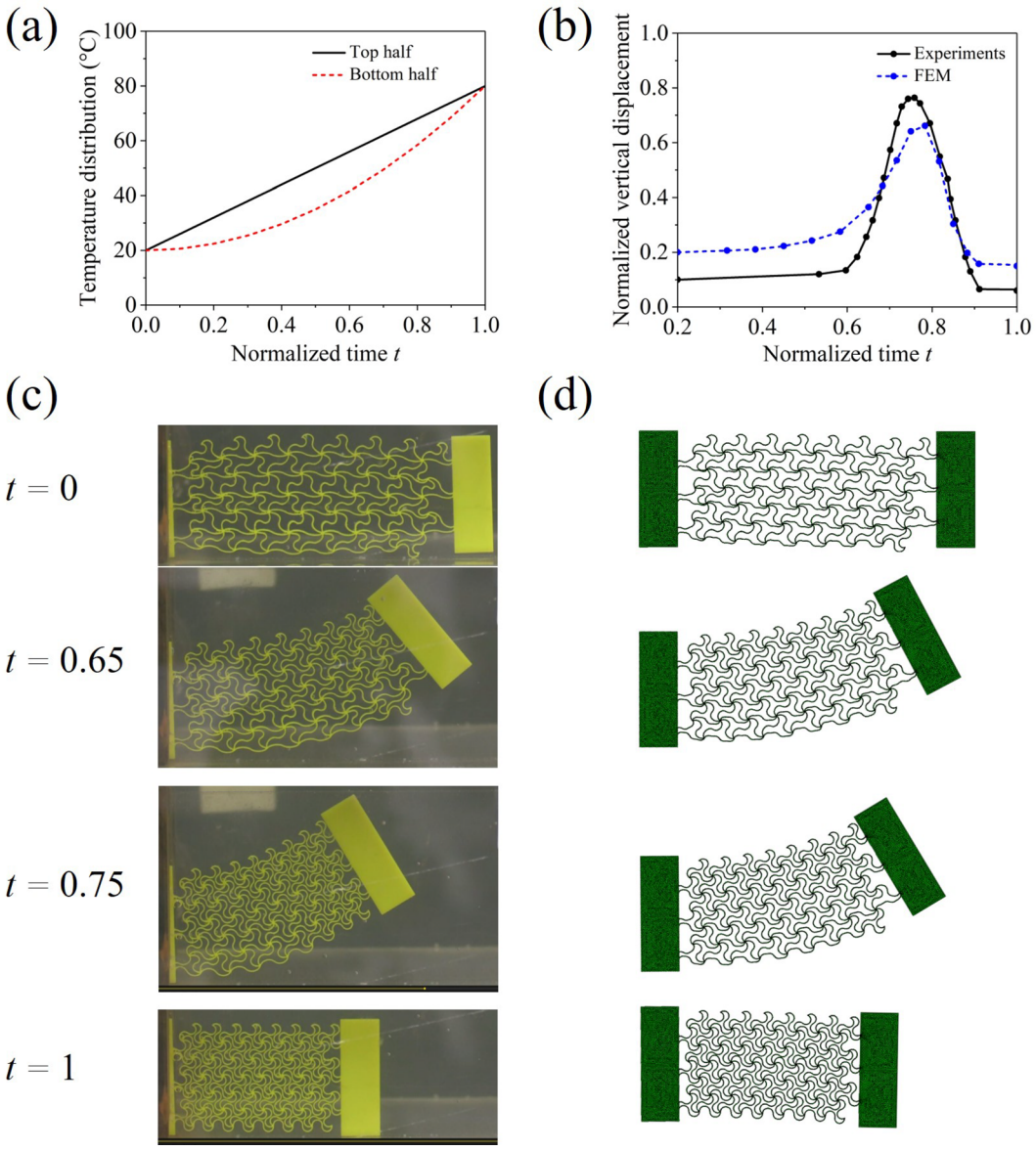

Figure 5. Bending of the triangular lattice subjected to non-uniform heating. (a) Change of temperature distribution at the top and bottom halves of the triangular lattice with normalized time t at the recovery step. (b) Quantitative comparisons of the experimental and FE simulated vertical displacements of the lattice normalized by the height of the lattice with t. (c) Experiments and (d) FE simulations both showing that the lattice undergoes bending deformation when subjected to a non-uniform heating in the recovery step.

Design of the Auxetic Structures. Auxetic structures, i.e., structures with negative Poisson's ratios, are designed as shown in Figure 4. The theoretically predicted, FE simulated, and experimental recovery shapes of the preprogrammed triangular horseshoe lattice structures are plotted at various temperatures T = 45, 63, and 70 °C in the recovery step (Supporting Information Videos 3 and 4). Figure 4d compares the deformed shapes of the theoretical, FE simulated, and expeirmental periodical units in the triangular lattice. The geometrical parameters of the microstructures are the same as those used in rectangular horseshoe lattices. It can be observed that the triangular lattice structures show auxetic behaviors, where the structure expands at the transverse direction when stretched in the axial direction. In order to quantitatively investigate the auxetic behavior, both the theoretical and experimental horizontal and vertical strains are plotted against temperature in Figure 4e,f. It can be seen that the vertical strain has the same sign with the horizontal strain, indicating that they expand or contract at the same time. Thus, the lattice exhibits positive Poisson's ratio. The experimental horizontal strain agrees reasonably with the theoretical prediction, while a small lag on the temperature exists. This lag is due to the viscoelasticity of the Vero material. There exists some discrepancy between the experimental and theoretical vertical strain, especially at lower temperatures. It may result from the boundary effect which is neglected in the theoretical model.

The effects of L on the Poisson's ratio of the triangular lattice are plotted in Figure 4g. The programming stress is 5 kPa. It can be seen that (1) the Poisson's ratio is always negative, (2) the magnitudes of the Poisson's ratios increase with the increase of L, and (3) the magnitudes of the Poisson's ratios decrease with the increase of T at the recovery step, especially at $T \cong T_g$. For example, the magnitudes of the Poisson's ratios increase from 0.2 to 0.35 as L/w increases from

https://dx.doi.org/10.1021/acsami.0c04097
ACS Appl. Mater. Interfaces 2020, 12, 22146−22156

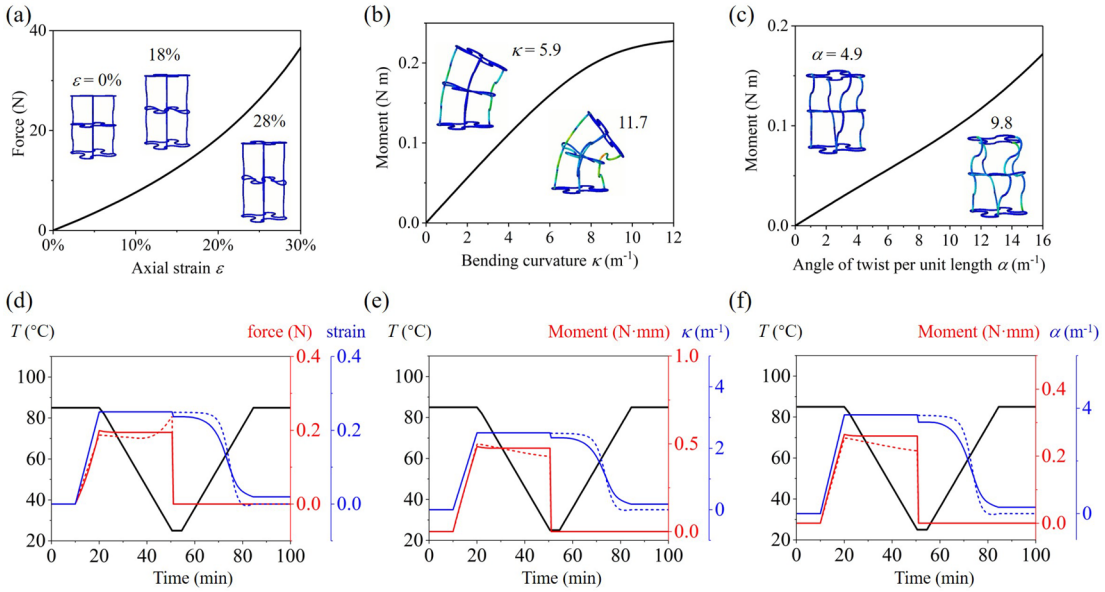

Figure 6. Shape memory behaviors of a 1 × 1 × 2 3D horseshoe lattice. (a–c) Loading–displacement curves of the lattice structure under axial, bending, and twisting loadings at room temperature, respectively. Insets show the deformed shapes at different strains. (d–f) Theoretical (dashed curves) and FE simulated (solid curves) shape memory behaviors of the 3D horseshoe structure programmed by axial, bending, and twisting loadings in strain control mode, respectively.

0 to 5 at T = 26 °C in the recovery step. As T increases from 50 to 70 °C, the magnitudes of Poisson's ratios decrease from ∼0.46 to ∼0.34.

Design of Intermediate Shapes by Inhomogeneous Stimulus. By applying a non-uniform stimulus in the recovery step, the shape recovery of the horseshoe lattice can be designed. For example, the experiments and FE simulations are conducted for a prestretched triangular lattice subjected to a temperature gradient as shown in Figure 5 (Supporting Information Videos 5 and 6). In the experiment, the temperature of the water in the tank where the lattice is immersed is higher at the top area and decreases continuously toward the bottom, and thus generates a temperature gradient on the lattice structures. During the recovery step in the FE simulation, the temperature at the top half of the lattice is set to increase linearly, while that at the bottom half is set to increase quadratically, as shown in Figure 5a. t is normalized by the whole time in the recovery step. It can be observed that the triangular units at the upper rows (higher temperature regions) recover faster than those at the bottom (lower temperature regions), and therefore the lattice bends toward higher temperature directions. As the temperature increases again, the whole structure reaches the rubbery state and the triangular lattice recovers to its initial un-deformed state. The experimental vertical displacement is quantitatively compared with that in the FE simulation. The vertical displacement normalized by the height of the lattice structure is plotted against the normalized time t in Figure 5b. Both the experiment and FE simulation show that the lattice undergoes a large vertical displacement at $t \sim 0.75$.

Design of 3D Horseshoe Lattice. In this section, the shape memory behaviors of a 3D horseshoe lattice under axial, bending, and twisting loadings are investigated. The unit structure of the 3D horseshoe lattice is made by replacing the straight edge of a cube with single horseshoe structure as shown in Figure 1b. The geometrical parameters of the horseshoe structure are R = 10 mm and L = 0. The cross-section of the horseshoe structure is a circle with the radius r = 1 mm. For the 3D lattice, the relation between the normalized loading and displacement under axial, bending and twisting loadings can be represented by

$$F_a(T, \epsilon) = E(T) f_a(\epsilon), \quad M_b(T, \kappa) = E(T) f_b(\kappa), \quad \text{and} \quad M_t(T, \alpha) = E(T) f_t(\alpha) \tag{10}$$

where $F_a(T,\epsilon)$, $M_b(T,\kappa)$, and $M_t(T,\alpha)$ are the applied axial force and the bending and twisting moments, respectively; ϵ is the axial strain; κ is the bending curvature; α is the angle of twist per unit length; and $f_a(\epsilon)$, $f_b(\kappa)$, and $f_t(\alpha)$ characterize the dependences of the axial force and bending and twisting moments normalized by the modulus $E(T)$ on ϵ, κ, and α, respectively. By replacing eq 1 with the above relations, their shape memory behaviors under axial, bending, or twisting loading can be studied using the developed theoretical model.

Since $f_a(\epsilon)$, $f_b(\kappa)$, and $f_t(\alpha)$ are difficult to directly calculate using the theoretical method, we use the FEM to obtain the simulation values at room temperature T = 25 °C with E = 1.2 GPa. Panels a–c of Figure 6 shows the loading–displacement curves of the 3D horseshoe under axial, bending and twisting loadings in FEM simulations (Supporting Information Video 7). A simple 1 × 1 × 2 structure (1 unit in x direction, 1 unit in y direction, and 2 units in z direction) is used. It can be seen that there is a strain–stiffening effect when the 3D horseshoe is under axial loading; i.e., the modulus of the structure increases with the increase of axial strain ϵ. On the contrary, the bending modulus decreases with the increase of the bending curvature κ. The twisting modulus remains almost a constant with a small increase when the twist is large.

The $f_a(\epsilon)$, $f_b(\kappa)$, and $f_t(\alpha)$ in the axial, bending, and twisting loadings are then incorporated into the theoretical framework to study the shape memory behaviors of the 1 × 1 × 2 3D horseshoe structure under axial, bending, and twisting loadings, respectively. The theoretical shape memory behaviors under strain control mode are shown in Figure 6d–f in dashed

https://dx.doi.org/10.1021/acsami.0c04097
ACS Appl. Mater. Interfaces 2020, 12, 22146–22156

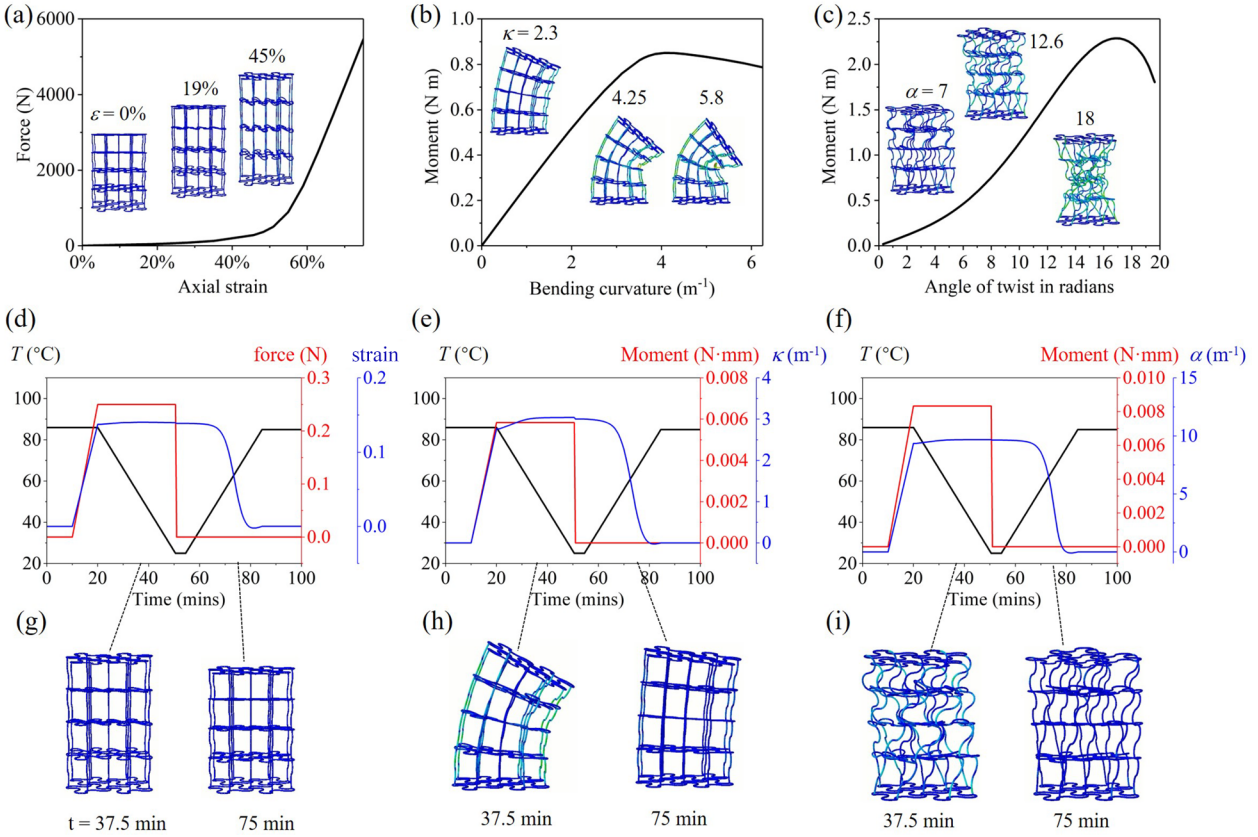

Figure 7. Shape memory behaviors of a 2 × 2 × 4 3D horseshoe lattice. (a–c) Loading–displacement relations of the lattice under axial, bending, and twisting loadings at room temperature. Insets show the deformed shapes are various strains. (d–f) Theoretical predicted shape memory behaviors of the lattice programmed by axial, bending, and twisting loadings in stress control mode. (g–i) Corresponding predicted shapes at t = 37.5 (T = 51 °C in the cooling step) and 75 min (T = 66 °C in the recovery step), respectively.

curves. Strain control mode is used. The shape memory behaviors of the same 3D structure are also studied by FEM simulations as shown in the solid curves to validate the theoretical model (Supporting Information Video 8). It should be noted that, even for this simple 1 × 1 × 2 structure, the computation cost to study the shape memory effect in FEM is quite large. The theoretical results and the FEM results agree reasonably well. However, there are some discrepancies. The change of the loading and displacement in the theoretical model is sharper than those in the FEM simulations. The reason could be the use of a phase evolution model in the theoretical modeling, in contrast to the use of the multibranch model in the FEM simulation. In the multibranch rheological model, the behavior of the polymer depends on time and the response is smoother.

The incorporation of the loading–displacement relation in FEM in room temperature to the theoretical framework could predict the shape memory behavior of the 3D lattice structure. This method of combining the FEM and theoretical framework significantly reduces the computational cost, and thus the prediction of the shape memory behaviors of more complex structure is made possible. For example, the shape memory behavior of 2 × 2 × 4 3D horseshoe lattice is constructed in Figure 7. The loading–displacement in room temperature under axial, bending, and twisting is investigated using the FEM as shown in Figure 7a–c (Supporting Information Video 9). The normalized loading–displacement relations $f_a(\epsilon)$, $f_b(\kappa)$, and $f_t(\alpha)$ are then fitted by a fifth-order polynomial function and incorporated into the theoretical framework to study their shape memory behaviors. The shape memory behaviors under axial, bending, and twisting programming are plotted in Figure 7d–f. The corresponding deformed shapes at t = 37.5 (T = 51 °C in the cooling step) and 75 min (T = 66 °C in the recovery step) are plotted in Figure 7g–i.

Comparing to the shape memory behavior of 2D lattice, the behavior of 3D structures under inhomogeneous heating is more complex. In order to investigate this process, the whole deformation in the shape recovery under inhomogeneous heating can be separated into two steps. The first step is the shape recovery without any constraint. In this step, the parts subjected to the same heating are recovered freely. Thus, the change of the shape may be continuous, and the shapes may not be compatible; i.e., the parts with different heating may overlap, or voids may exist between them. At the second step, an elastic deformation is introduced to maintain compatibility. As shown in Figure S9, the first step maps (a) the shape at T_H to (c) a virtual configuration which is locally stress-free. The elastic deformation then maps the (c) virtual configuration to (b) the recovered shape in order to maintain continuity of the structures. The overall deformation is the composition of the deformations in the two steps. The deformed shapes and modulus of the structures in the first step can be calculated using the theoretical framework. The second step still needs the use of FEM, especially for complex structure and heating.

In this work, the phase evolution model is used to obtain the analytical solutions for lattice structure. The development of the analytical solutions significantly reduces the computational cost and facilitates the inverse design of the programmable

https://dx.doi.org/10.1021/acsami.0c04097
ACS Appl. Mater. Interfaces 2020, 12, 22146–22156

shape changing behavior. Comparing to the phase evolution model, the multibranch rheological model is more accurate and the dependence of the polymer behaviors on time is taken into account by the introduction of the viscoelastic dashpot in the branches. But the analytical solutions would be difficult to be obtained. From Figure 6d–f, it can be seen that the shape changing behaviors predicted by the multibranch model are smoother (solid curves obtained by FEM simulations alone) than those predicted by the phase evolution model (dashed curves obtained by combining FEM and theoretical model). The use of the multibranch model to predict the shape changing of the 3D lattice would be interesting and worth studying in the future.

CONCLUSION

In summary, we study the shape changes of 3D printed lattice structures under a thermal stimulus by a combination of experiments and theory and FE simulations. The shape changing behaviors of the 2D rectangular and triangule horseshoe lattice structures and 3D horseshoe lattice are shown as an example. The theoretical model is developed on the basis of the phase evolution and can accurately capture the lattices' shape changes. In contrast to the usual linear stress–strain behavior, a function is used to characterize the nonlinear stress–strain behaviors of the lattice structure resulting from the geometrical nonlinearity. We develop an analytical phase evolution model to predict the shape memory effects of 3D printed lattice structures under both strain and stress control mode. With the developed model, we design the shape changes of 3D printed rectangular/triangular modified horseshoe lattice structures that can exhibit large controllable deformations subjected to a thermal stimulus. By combining the loading–displacement behaviors of 3D lattices obtained in FEM and the theoretical method, the shape change of 3D lattice under axial, bending, or twisting loading can also be predicted. Thus, it provides a general framework to design the shape memory effect of 3D lattice. We fabricate the designed rectangular/triangular horseshoe lattices and conduct FEM simulation to validate the theoretical model. All of the theoretical, experimental, and FE simulated results agree well, which proves the effectiveness of the theoretical method. By combining experiments, theoretical modeling, and FE simulation, this work helps to illustrate the deformation mechanism of 3D printed shape changing lattice structures and provides theoretical guidelines for the design of 3D printed programmable lattice structures.

ASSOCIATED CONTENT

Supporting Information

The Supporting Information is available free of charge at https://pubs.acs.org/doi/10.1021/acsami.0c04097.

Theoretical models, thermomechanical constitutive behavior, experimental details, finite element methods, shape memory recovery modeling, and effect of heating rate (PDF)

Video S1 showing rectangular lattice–FEM simulation (MP4)

Video S2 showing rectangular lattice-experiment (MP4)

Video S3 showing triangular lattice–FEM simulation (MP4)

Video S4 showing triangular lattice-experiment (MP4)

Video S5 showing bending of triangular lattice–FEM simulation (MP4)

Video S6 showing bending of triangular lattice-experiment (MP4)

Video S7 showing axial loading, bending, and twisting of 1 × 1 × 2 3D horseshoe structure at room temperature (MP4)

Video S8 showing shape memory effect of a 1 × 1 × 2 3D horseshoe structure programmed by axial, bending, and twisting load (MP4)

Video S9 showing axial loading, bending, and twisting of 2 × 2 × 4 3D horseshoe structure at room temperature (MP4)

AUTHOR INFORMATION

Corresponding Author

Guoying Gu – *Robotics Institute and State Key Laboratory of Mechanical System and Vibration, School of Mechanical Engineering, Shanghai Jiao Tong University, Shanghai 200240, China;* orcid.org/0000-0002-7778-4523; Email: guguoying@sjtu.edu.cn

Authors

Dong Wang – *Robotics Institute and State Key Laboratory of Mechanical System and Vibration, School of Mechanical Engineering, Shanghai Jiao Tong University, Shanghai 200240, China;* orcid.org/0000-0002-8569-8713

Haipeng Xu – *Robotics Institute and State Key Laboratory of Mechanical System and Vibration, School of Mechanical Engineering, Shanghai Jiao Tong University, Shanghai 200240, China*

Jinqiang Wang – *Robotics Institute and State Key Laboratory of Mechanical System and Vibration, School of Mechanical Engineering, Shanghai Jiao Tong University, Shanghai 200240, China*

Chengru Jiang – *Robotics Institute and State Key Laboratory of Mechanical System and Vibration, School of Mechanical Engineering, Shanghai Jiao Tong University, Shanghai 200240, China*

Xiangyang Zhu – *Robotics Institute and State Key Laboratory of Mechanical System and Vibration, School of Mechanical Engineering, Shanghai Jiao Tong University, Shanghai 200240, China*

Qi Ge – *Department of Mechanical and Energy Engineering, Southern University of Science and Technology, Shenzhen 518055, China;* orcid.org/0000-0002-8666-8532

Complete contact information is available at: https://pubs.acs.org/10.1021/acsami.0c04097

Notes

The authors declare no competing financial interest.

ACKNOWLEDGMENTS

D.W. acknowledges the support by the National Natural Science Foundation of China (Grant No. 51905336) and the Shanghai Sailing Program (Grant No. 19YF1423000). G.G. acknowledges the support by the National Natural Science Foundation of China (Grant Nos. 91848204 and 91948302) and the Shanghai Jiao Tong University Scientific and Technological Innovation Funds (2019QYB08). Q.G. acknowledges the Research Project of State Key Laboratory of

https://dx.doi.org/10.1021/acsami.0c04097
ACS Appl. Mater. Interfaces 2020, 12, 22146–22156

Mechanical System, and Vibration MSV201802 by Shanghai Jiao Tong University.

REFERENCES

(1) Silverberg, J. L.; Evans, A. A.; McLeod, L.; Hayward, R. C.; Hull, T.; Santangelo, C. D.; Cohen, I. Using Origami Design Principles To Fold Reprogrammable Mechanical Metamaterials. *Science* **2014**, *345*, 647−650.
(2) Liu, J.; Gu, T.; Shan, S.; Kang, S. H.; Weaver, J. C.; Bertoldi, K. Harnessing Buckling To Design Architected Materials That Exhibit Effective Negative Swelling. *Adv. Mater.* **2016**, *28*, 6619−6624.
(3) Schenk, M.; Guest, S. D. Geometry Of Miura-Folded Metamaterials. *Proc. Natl. Acad. Sci. U. S. A.* **2013**, *110*, 3276−3281.
(4) Yasuda, H.; Yang, J. Reentrant Origami-Based Metamaterials With Negative Poisson'S Ratio And Bistability. *Phys. Rev. Lett.* **2015**, *114*, 185502.
(5) Bertoldi, K.; Vitelli, V.; Christensen, J.; van Hecke, M. Flexible Mechanical Metamaterials. *Nat. Rev. Mater.* **2017**, *2*, 17066.
(6) Cummer, S. A.; Christensen, J.; Alù, A. Controlling Sound With Acoustic Metamaterials. *Nat. Rev. Mater.* **2016**, *1*, 16001.
(7) Zheng, X.; Lee, H.; Weisgraber, T. H.; Shusteff, M.; DeOtte, J.; Duoss, E. B.; Kuntz, J. D.; Biener, M. M.; Ge, Q.; Jackson, J. A.; Kucheyev, S. O.; Fang, N. X.; Spadaccini, C. M. Ultralight, Ultrastiff Mechanical Metamaterials. *Science* **2014**, *344*, 1373−1377.
(8) Zadpoor, A. A. Mechanical Meta-Materials. *Mater. Horiz.* **2016**, *3*, 371−381.
(9) Kowsari, K.; Akbari, S.; Wang, D.; Fang, N. X.; Ge, Q. High-Efficiency High-Resolution Multimaterial Fabrication For Digital Light Processing-Based Three-Dimensional Printing. *3D Printing and Additive Manufacturing* **2018**, *5*, 185−193.
(10) Yuan, C.; Kowsari, K.; Panjwani, S.; Chen, Z.; Wang, D.; Zhang, B.; Ng, C. J.-X.; Alvarado, P. V. y.; Ge, Q. Ultrafast Three-Dimensional Printing Of Optically Smooth Microlens Arrays By Oscillation-Assisted Digital Light Processing. *ACS Appl. Mater. Interfaces* **2019**, *11*, 40662−40668.
(11) Kuang, X.; Roach, D. J.; Wu, J.; Hamel, C. M.; Ding, Z.; Wang, T.; Dunn, M. L.; Qi, H. J. Advances in 4D printing: Materials and applications. *Adv. Funct. Mater.* **2019**, *29*, 1805290.
(12) Gladman, A. S.; Matsumoto, E. A.; Nuzzo, R. G.; Mahadevan, L.; Lewis, J. A. Biomimetic 4d Printing. *Nat. Mater.* **2016**, *15*, 413−418.
(13) Ding, Z.; Yuan, C.; Peng, X.; Wang, T.; Qi, H. J.; Dunn, M. L. Direct 4d Printing Via Active Composite Materials. *Science advances* **2017**, *3*, No. e1602890.
(14) Wagner, M.; Chen, T.; Shea, K. Large Shape Transforming 4d Auxetic Structures. *3D Printing and Additive Manufacturing* **2017**, *4*, 133−142.
(15) Ding, Z.; Weeger, O.; Qi, H. J.; Dunn, M. L. 4d Rods: 3d Structures Via Programmable 1d Composite Rods. *Mater. Des.* **2018**, *137*, 256−265.
(16) Manti, M.; Cacucciolo, V.; Cianchetti, M. Stiffening In Soft Robotics: A Review Of The State Of The Art. *IEEE Robotics & Automation Magazine* **2016**, *23*, 93−106.
(17) Kuang, X.; Wu, J.; Chen, K.; Zhao, Z.; Ding, Z.; Hu, F.; Fang, D.; Qi, H. J. Grayscale Digital Light Processing 3d Printing For Highly Functionally Graded Materials. *Science advances* **2019**, *5*, No. eaav5790.
(18) Wang, L.; Wang, D.; Huang, S.; Guo, X.; Wan, G.; Fan, J.; Chen, Z. Controllable Shape Changing And Tristability Of Bilayer Composite. *ACS Appl. Mater. Interfaces* **2019**, *11*, 16881−16887.
(19) Ge, Q.; Dunn, C. K.; Qi, H. J.; Dunn, M. L. Active Origami By 4d Printing. *Smart Mater. Struct.* **2014**, *23*, No. 094007.
(20) Ge, Q.; Sakhaei, A. H.; Lee, H.; Dunn, C. K.; Fang, N. X.; Dunn, M. L. Multimaterial 4d Printing With Tailorable Shape Memory Polymers. *Sci. Rep.* **2016**, *6*, 31110.
(21) Lei, M.; Hong, W.; Zhao, Z.; Hamel, C.; Chen, M.; Lu, H.; Qi, H. J. 3d Printing Of Auxetic Metamaterials With Digitally Reprogrammable Shape. *ACS Appl. Mater. Interfaces* **2019**, *11*, 22768−22776.
(22) Kuang, X.; Chen, K.; Dunn, C. K.; Wu, J.; Li, V. C.; Qi, H. J. 3d Printing Of Highly Stretchable, Shape-Memory, And Self-Healing Elastomer Toward Novel 4d Printing. *ACS Appl. Mater. Interfaces* **2018**, *10*, 7381−7388.
(23) Wei, H.; Zhang, Q.; Yao, Y.; Liu, L.; Liu, Y.; Leng, J. Direct-Write Fabrication Of 4d Active Shape-Changing Structures Based On A Shape Memory Polymer And Its Nanocomposite. *ACS Appl. Mater. Interfaces* **2017**, *9*, 876−883.
(24) Ambulo, C. P.; Burroughs, J. J.; Boothby, J. M.; Kim, H.; Shankar, M. R.; Ware, T. H. Four-Dimensional Printing Of Liquid Crystal Elastomers. *ACS Appl. Mater. Interfaces* **2017**, *9*, 37332−37339.
(25) Yang, C.; Boorugu, M.; Dopp, A.; Ren, J.; Martin, R.; Han, D.; Choi, W.; Lee, H. 4d Printing Reconfigurable, Deployable And Mechanically Tunable Metamaterials. *Mater. Horiz.* **2019**, *6*, 1244−1250.
(26) Cheng, N. G.; Gopinath, A.; Wang, L.; Iagnemma, K.; Hosoi, A. E. Thermally Tunable, Self-Healing Composites For Soft Robotic Applications. *Macromol. Mater. Eng.* **2014**, *299*, 1279−1284.
(27) Zhang, Y.-F.; Zhang, N.; Hingorani, H.; Ding, N.; Wang, D.; Yuan, C.; Zhang, B.; Gu, G.; Ge, Q. Fast-Response, Stiffness-Tunable Soft Actuator By Hybrid Multimaterial 3d Printing. *Adv. Funct. Mater.* **2019**, *29*, 1806698.
(28) Li, W.-B.; Zhang, W.-M.; Zou, H.-X.; Peng, Z.-K.; Meng, G. Bioinspired Variable Stiffness Dielectric Elastomer Actuators With Large And Tunable Load Capacity. *Soft robotics* **2019**, *6*, 631−643.
(29) Sofla, A.; Meguid, S.; Tan, K.; Yeo, W. Shape Morphing Of Aircraft Wing: Status And Challenges. *Mater. Eng.* **2010**, *31*, 1284−1292.
(30) Jenett, B.; Calisch, S.; Cellucci, D.; Cramer, N.; Gershenfeld, N.; Swei, S.; Cheung, K. C. Digital Morphing Wing: Active Wing Shaping Concept Using Composite Lattice-Based Cellular Structures. *Soft robotics* **2017**, *4*, 33−48.
(31) Rossiter, J.; Takashima, K.; Scarpa, F.; Walters, P.; Mukai, T. Shape Memory Polymer Hexachiral Auxetic Structures With Tunable Stiffness. *Smart Mater. Struct.* **2014**, *23*, No. 045007.
(32) Florijn, B.; Coulais, C.; van Hecke, M. Programmable Mechanical Metamaterials. *Phys. Rev. Lett.* **2014**, *113*, 175503.
(33) Mirzaali, M.; Janbaz, S.; Strano, M.; Vergani, L.; Zadpoor, A. A. Shape-Matching Soft Mechanical Metamaterials. *Sci. Rep.* **2018**, *8*, 965.
(34) Florijn, B.; Coulais, C.; van Hecke, M. Programmable Mechanical Metamaterials: The Role Of Geometry. *Soft Matter* **2016**, *12*, 8736−8743.
(35) Rafsanjani, A.; Akbarzadeh, A.; Pasini, D. Snapping Mechanical Metamaterials Under Tension. *Adv. Mater.* **2015**, *27*, 5931−5935.
(36) Ma, Q.; Cheng, H.; Jang, K.-I.; Luan, H.; Hwang, K.-C.; Rogers, J. A.; Huang, Y.; Zhang, Y. A Nonlinear Mechanics Model Of Bio-Inspired Hierarchical Lattice Materials Consisting Of Horseshoe Microstructures. *J. Mech. Phys. Solids* **2016**, *90*, 179−202.
(37) Wang, D.; Xiong, Y.; Zhang, B.; Zhang, Y.-F.; Rosen, D.; Ge, Q. Design Framework For Mechanically Tunable Soft Biomaterial Composite Enhanced By Modified Horseshoe Lattice Structures. *Soft Matter* **2020**, *16*, 1473−1484.
(38) Hawkes, E.; An, B.; Benbernou, N. M.; Tanaka, H.; Kim, S.; Demaine, E.; Rus, D.; Wood, R. J. Programmable Matter By Folding. *Proc. Natl. Acad. Sci. U. S. A.* **2010**, *107*, 12441−12445.
(39) Wei, Z. Y.; Guo, Z. V.; Dudte, L.; Liang, H. Y.; Mahadevan, L. Geometric Mechanics Of Periodic Pleated Origami. *Phys. Rev. Lett.* **2013**, *110*, 215501.
(40) Hong, W.; Liu, Z.; Suo, Z. Inhomogeneous Swelling Of A Gel In Equilibrium With A Solvent And Mechanical Load. *Int. J. Solids Struct.* **2009**, *46*, 3282−3289.

https://dx.doi.org/10.1021/acsami.0c04097
ACS Appl. Mater. Interfaces 2020, 12, 22146−22156